

Melanoma-associated repair-like Schwann cells suppress anti-tumor T-cells via 12/15-LOX/COX2-associated eicosanoid production

Oleg Kruglov^a, Kavita Vats^a, Vishal Soman^b, Vladimir A. Tyurin^c, Yulia Y. Tyurina^c, Jiefei Wang^b, Li'an Williams^a, Jiyang Zhang^a, Cara Donahue Carey^a, Erik Jaklitsch^d, Uma R. Chandran^b, Hülya Bayir^{c,e,f}, Valerian E. Kagan, and ^cYuri L. Bunimovich^{a,g}

^aDepartment of Dermatology, University of Pittsburgh School of Medicine, Pittsburgh, PA, USA; ^bDepartment of Biomedical Informatics, University of Pittsburgh School of Medicine, Pittsburgh, PA, USA; ^cCenter for Free Radical and Antioxidant Health, Department of Environmental Health and Occupational Health, University of Pittsburgh, Pittsburgh, PA, USA; ^dSchool of Medicine, University of Pittsburgh, Pittsburgh, PA, USA; ^eSafar Center for Resuscitation Research, Department of Critical Care Medicine, University of Pittsburgh, Pittsburgh, PA, USA; ^fChildren's Neuroscience Institute, UPMC Children's Hospital of Pittsburgh, Pittsburgh, PA, USA; ^gHillman Cancer Institute, University of Pittsburgh Medical Center, Pittsburgh, PA, USA

ABSTRACT

Peripheral glia, specifically the Schwann cells (SCs), have been implicated in the formation of the tumor microenvironment (TME) and in cancer progression. However, *in vivo* and *ex vivo* analyses of how cancers reprogram SC functions in different organs of tumor-bearing mice are lacking. We generated P1p1-CreERT/tdTomato mice which harbor fluorescently labeled myelinated and non-myelin forming SCs. We show that this model enables the isolation of the SCs with high purity from the skin and multiple other organs. We used this model to study phenotypic and functional reprogramming of the SCs in the skin adjacent to melanoma tumors. Transcriptomic analyses of the peritumoral skin SCs versus skin SCs from tumor-free mice revealed that the former existed in a repair-like state typically activated during nerve and tissue injury. Peritumoral skin SCs also downregulated pro-inflammatory genes and pathways related to protective anti-tumor responses. *In vivo* and *ex vivo* functional assays confirmed immunosuppressive activities of the peritumoral skin SCs. Specifically, melanoma-reprogrammed SCs upregulated 12/15-lipoxygenase (12/15-LOX) and cyclooxygenase (COX)-2, and increased production of anti-inflammatory polyunsaturated fatty acid (PUFA) metabolites prostaglandin E2 (PGE2) and lipoxins A4/B4. Inhibition of 12/15-LOX or COX2 in SCs, or EP4 receptor on lymphocytes reversed SC-dependent suppression of anti-tumor T-cell activation. Therefore, SCs within the skin adjacent to melanoma tumors demonstrate functional switching to repair-like immunosuppressive cells with dysregulated lipid oxidation. Our study suggests the involvement of the melanoma-associated repair-like peritumoral SCs in the modulation of locoregional and systemic anti-tumor immune responses.

ARTICLE HISTORY

Received 24 July 2022
Revised 12 March 2023
Accepted 13 March 2023



KEYWORDS

Cancer; melanoma; neuroimmunology; Schwann cell; tumor microenvironment


Introduction

The peripheral nervous system (PNS) is an important component of the tumor microenvironment (TME).¹ Autonomic and sensory neurons impact the progression of cancers of the prostate,² pancreas,³ skin,⁴ and other organs.^{5,6} The Schwann cells (SCs), principal neuroglia of the PNS, also promote tumor growth and cancer cell invasion through various mechanisms.⁷⁻¹⁷ While SCs are tasked with the maintenance of PNS homeostasis, they exhibit remarkable plasticity in disease states and after nerve injury.¹⁸ We recently linked pro-tumor activities of melanoma-associated SCs with their intrinsic responsiveness to nerve injury, presumably induced locally in the TME and the peritumoral skin by the growing tumor.¹⁰ Subsequently, repair-like activation of SCs has been confirmed in other malignancies, including pancreatic and lung cancers.^{9,17,19-21} SCs have been shown to promote cancer

progression via a direct crosstalk with malignant cells and, indirectly, via the neuroimmune axis. Interactions between SCs and cancer cells can facilitate epithelial-to-mesenchymal transition of the latter, cancer cell dispersion and perineural invasion.^{7,14,17,20,22,23} Immunomodulatory functions of SCs, including chemoattraction and polarization of the immune cells, may also support cancer by enforcing immune tolerance and immunosuppression.^{10,11,24-26} As most studies of SCs in cancer to date employed *ex vivo* SC manipulation and analytical methods, the *in-vivo* evidence of tumor-directed SC reprogramming and immunomodulation, and their relevance to cancer progression is still lacking. We previously showed that peritumoral SCs in clinical melanoma specimens upregulate markers of activated/trans-differentiated repair-like state and co-localize with skin-infiltrating immune cells.^{10,24} To better define phenotypic and functional characteristics of the peritumoral SCs *in vivo*, we utilized a syngeneic melanoma-

CONTACT Yuri L. Bunimovich  bunimovichyl@upmc.edu  Department of Dermatology, University of Pittsburgh Medical Center, 200 Lothrop Street E1157 Thomas E. Starzl Biomedical Science Tower, Pittsburgh, PA 15213, USA

KV and OK contributed equally to this work.

 Supplemental data for this article can be accessed online at <https://doi.org/10.1080/2162402X.2023.2192098>

© 2023 The Author(s). Published with license by Taylor & Francis Group, LLC.

This is an Open Access article distributed under the terms of the Creative Commons Attribution-NonCommercial License (<http://creativecommons.org/licenses/by-nc/4.0/>), which permits unrestricted non-commercial use, distribution, and reproduction in any medium, provided the original work is properly cited. The terms on which this article has been published allow the posting of the Accepted Manuscript in a repository by the author(s) or with their consent.

bearing genetically labeled SC murine model. RNA-seq analyses of sorted peritumoral skin SCs (psSCs) revealed significant changes in their transcriptional profiles compared to control SCs (cSCs) isolated from the skin of tumor-free mice. Specifically, psSCs adjacent to melanoma tumors demonstrated an enhanced cell-cycle activity and an immature, stem-like phenotype, as well as downregulated pro-inflammatory pathways. *In vivo* and *ex vivo* functional analyses demonstrated that dysregulated lipid oxidation of melanoma-associated repair-like psSCs leads to 12/15-LOX/COX2-dependent increase in their production of immunosuppressive oxygenated PUFA eicosanoid metabolites PGE2 and lipoxins, which dampen anti-tumor effector T-cell responses. Our results directly implicate tumor-associated reprogrammed repair-like cutaneous SCs in the suppression of protective anti-melanoma immune responses.

Materials and methods

Animal models

B6.Cg-Tg(Plp1-cre/ERT) mice (Stock No: 005975), B6.Cg-Gt(ROSA)26Sor^{tm14(CAG-tdTomato)} mice (Stock No: 007914), B6.129S2-Alox15^{tm1Fun/J} mice (Stock No: 002778), and C57Bl/6 mice were purchased from the Jackson Laboratory. Genotyping was performed using tail snips, and DNA was extracted using a direct lysis buffer kit (Viagen Biotech). Gene-specific primers for the detection of Plp1-Cre and tdTomato transgenes are listed in the Supplementary Table S1. To induce Cre recombination, tamoxifen (Sigma) in corn oil (20 mg/mL) was injected intraperitoneally (75 mg/kg) every 24 h for five consecutive days. To initiate melanomas, mice were anesthetized with isoflurane (Covetrus), using single animal vaporizer unit (E-Z Systems, 108SA) at a flow rate of 2 L/min, and injected intradermally with B16F10 cells (10^5 cells in 100 μ L sterile PBS) into the dorsolateral skin. Fourteen days after injections, tumors and other organs were harvested. All studies were conducted in accordance with the NIH guidelines for the Care and Use of Laboratory Animals and approved by the Institutional Animal Care and Use Committee of the University of Pittsburgh (Pittsburgh, PA)

Primary cells and cell lines

Primary tdTomato+p75^{NTR+} SCs were isolated by FACS from fresh skin or sciatic nerves according to a previously described protocol and cultured in SC medium (ScienCell) with 1% (v/v) SC growth supplement (ScienCell), 1% (v/v) penicillin/streptomycin solution, and 5% FBS at 37C, 5% CO₂.^{7,26} Briefly, sciatic nerves were dissected under sterile conditions, incubated in SC medium at 37C for 5 days, dissociated using 1 mg/mL NB4G collagenase (Sigma) in 3 mL HBSS at 37C for 45 min, cut into 1-mm segments and kept in NB4G collagenase at 37C for 30 min. After centrifugation (400 \times g, 5 min), pellets were resuspended in 1 mL SC medium, and the nerves were triturated until they were completely dissociated. Cells were placed in SC medium supplemented with 2 μ M forskolin (Sigma) and 50 ng/mL heregulin- β 1 (Sigma) and cultured in poly-D-lysine pre-coated flasks for 4 days followed by additional 7 days in SC

medium without forskolin and heregulin. During this time, SCs were separated twice from the fibroblasts using 300 μ g/mL collagenase NB4G solution in 6 mL HBSS at 37C for 30 min. B16F10 murine melanoma cells (ATCC) were cultured in RPMI-1640 (Cytiva), supplemented with 10% FBS (R&D Systems), 0.1% 2-Mercaptoethanol (Gibco), 1% Antibiotic Antimitotic Solution (Sigma), 1% HEPES (Gibco), 1% NEAA Mixture (Lonza, 13-114E), 1% L-Glutamine (Gibco). Cells were used at passages (P) 3–6 for intradermal injections.

Immunofluorescence (IF) microscopy

Tissues were fixed with 2% PFA for 2 h and incubated in 30% sucrose in PBS for 24 h. Tissues were frozen in 2-methylbutane (Sigma) in liquid nitrogen, embedded in Tissue Plus OCT (Thermo Fisher) and processed into 50 μ m thick sections. Sections were permeabilized with 0.1% Triton X-100 (Sigma) in PBS for 10 min, blocked with 5% goat serum (Gibco) + 2% BSA in PBS for 45 min and washed with 0.5% BSA in PBS containing 0.1% Triton X-100. Immunostaining was performed for 16 h at 4C with primary antibodies followed by secondary antibodies (Supplementary Table S2) for 1 h at RT and then 4',6-diamidino-2-phenylindole (DAPI, Sigma, 1 μ g/mL). Sections mounted in Gelvatol medium (Sigma) were imaged using Nikon A1+ confocal microscope at the Center for Biological Imaging (University of Pittsburgh, PA). Image analyses were performed with NIS-Elements AR 4.40 software (Nikon).

Flow cytometry and SC sorting

Single-cell suspensions were prepared from harvested organs, including skin, bone marrow, lymph nodes, spleen, liver, small intestine, DRG, sciatic and spinal nerves. Tissues were chopped into small pieces followed by incubation in DMEM (Corning) containing collagenase D (1 mg/mL, Sigma) and DNase (1 mg/mL, Sigma) for 45 min at 37C, and then filtered through 70 μ m cell strainers (Falcon). For flow analysis, obtained cell suspensions were centrifuged, washed twice with FACS buffer (MACS buffer, Miltenyi Biotec, 130-091-221), and incubated with primary antibodies against p75^{NTR} (Abcam, EP1039Y, 1:100), GAP43 (Abcam, EP890Y, 1:100), or S100 β (Abcam, EP1576Y, 1:100) for 1 h at 4C. Cells were washed twice with FACS buffer and incubated with secondary antibodies, goat-anti-rabbit IgG (conjugated with FITC, A11008, or APC, A21241, Invitrogen, 1:200) for 45 min at 4C. Cells were washed and resuspended in FACS buffer. Flow cytometry was performed on BD LSRFortessa (BD Biosciences), and data analyzed using FlowJo software (flowjo.com). To isolate SCs, cell suspensions obtained from digestions of dorsal skin and sciatic nerves were stained for p75^{NTR} as described above. SC sorting was performed on BD FACS Aria cell sorter using FACSDiva software (BD Biosciences), with 100 μ m nozzles at 20 psi sheath pressure. To profile intratumoral immune cells, 10⁴ FACS-purified SCs were mixed with 10⁵ B16F10 melanoma cells in sterile PBS and injected intradermally in C57Bl/6 mice (100 μ L). After 14 days, tumors were harvested, digested and filtered as described above. The resulting single-cell suspensions were fixed and permeabilized with the FoxP3/Transcription Factor Staining

kit (eBioscience) for 30 min at 20°C, incubated with conjugated surface antibodies for 60 min at 4°C, washed with PBS, and incubated with the conjugated intracellular antibodies for 60 min at 20°C (Supplementary Table S3). Flow cytometry was performed on BD LSRFortessa, and data analyzed using FlowJo software.

Interferon (IFN)- γ ELISA

Spleens from tumor-bearing C57Bl/6 mice were collected on day fourteen after intradermal injections of 10^5 B16F10 melanoma cells. Tissues were passed through a 70 μ m cell strainer, washed with PBS and incubated for 5 min at 4°C in 2 mL of RBC lysis buffer (Biolegend). Cells were centrifuged, and cultured (10^5 cells) for 7 days in RPMI containing 10% FBS, 100 U/mL penicillin, 100 μ g streptomycin, 2 mM L-glutamine, 50 μ M β -mercaptoethanol and 10 ng/mL human IL-15 (PeproTech) in 96-well plates with irradiated B16F10 cells (10^4 rad, Gammacell 1000 Elite, Nordion) at 20:1 ratio (splenocytes/melanoma cells). Cells were washed in PBS, counted, and co-incubated (10^5 cells) in RPMI (as above) for 24 h with B16F10 cells and the SCs (purified on the same day by FACS from skin or sciatic nerves of Plp1-Cre/tdTomato mice) at 10:1:2 ratio (splenocytes:B16:skin SCs), 10:1:0.5 (splenocytes:B16:nerve SCs). For T-cell enrichment, after 7-day incubation described above T-cells were purified from the activated splenocytes using Mouse Pan T Cell Isolation Kit II (Miltenyi), and 4×10^4 T-cells were co-incubated with B16F10 cells and SCs. When indicated, 12/15-LOX inhibitors (ML351 and PD146176, 2 μ M, Tocris), COX-2 inhibitor (SC236, 2 μ M, Tocris) and EP4 antagonist (ONO-AE3-208, 5 μ M, Tocris) were used. IFN- γ was determined in 10 μ L of supernatant (1:10 dilution) using mouse ELISA kit (BD Biosciences), based on standard curves obtained utilizing kit IFN γ , according to the manufacturer's protocol. Measurements were performed with iD5 plate reader (Molecular Devices) and analyzed using SoftMax Pro 7.1 (Molecular Devices).

Lipoxin B4 ELISA

SCs were isolated from sciatic nerves of 10-week-old C57Bl/6 or 12/15-LOX-deficient (B6.129S2-Alox15^{tm1Fun/J}) mice as described above. SCs were treated with B16F10-conditioned medium (50% v/v) or control medium for 24 h, washed, and cultured for 24 h in SC medium supplemented with 2% FBS. Lipoxin B4 concentrations were measured in SC supernatant (25 μ L) using ELISA Kit (Cayman Chemical).

Real-time (RT)-PCR

RNA was extracted immediately after SC sorting using RNeasy Micro Kit (Qiagen) per manufacturer's protocol, and quantified using DeNovix DS-11 spectrophotometer. For cDNA synthesis, 40 ng RNA was converted to cDNA using QuantiTect Reverse Transcription Kit (Qiagen). qRT-PCR was performed using Fast SYBR Green Master Mix (Applied Biosystems) with appropriate primers (Supplementary Table S4), and *Gapdh* as endogenous control. Reactions were

run and analyzed on StepOnePlus thermocycler (Applied Biosystems). Relative fold changes were calculated and normalized based on $2^{-\Delta\Delta C_t}$ method.

RNA-sequencing (RNA-seq)

Total RNA from FACS-purified SCs was isolated using RNeasy Micro Kit (Qiagen) as per the manufacturer's instructions. Quality and concentration of RNA were determined with Qubit (ThermoFisher) and Agilent Bioanalyzer (RIN 4.0–6.8), and 20 ng RNA per sample was used. Sequencing libraries were constructed by using Illumina® Stranded Total RNA Prep, Ligation with Ribo-Zero Plus (#20040525) with a read length of 2×75 bp. Approximately 542,959,211 total reads, paired end, were obtained (Illumina NextSeq 500/550 v2.5 Mid Output, 150 cycles). The reverse stranded paired-end RNA-Seq reads were checked for presence of adapters and high-quality bases using FastQC (v 0.11.9). The universal adapters in the high-quality reads were already trimmed, and therefore did not require the use of an adapter trimming tool. Due to the presence of a T-overhang from the sequencing machine, the Basespace FastQ Toolkit (v 2.2.5) was used to trim said overhang prior to alignment. Trimmed reads were mapped to the Ensembl mouse reference genome (GRCm38 mm10) with HISAT2 (v 2.1.0). The output file from HISAT2 was converted from SAM format to BAM format using SAMtools (v 1.10). Counts for expressed genes were generated using HT-Seq (v 0.11.2) and were then imported into the Bioconductor R package, edgeR (v 3.32.1) for differential expression (DE) analysis. DE genes that passed a cutoff (\log_2 of ± 1 , FDR 0.05), along with their differential expression values, were uploaded to Ingenuity Pathway Analysis (IPA, Redwood City, CA). Enrichr (maayanlab.cloud/Enrichr) pathway enrichment analyses were also performed. Bar charts were generated using R package ggplot2 (v 3.3.5). Heatmaps from gene set enrichment analyses were generated using Gene Set Enrichment Analysis (GSEA) (v. 4.2.2). To generate interactive networks, genes from selected IPA pathways were exported to STRING v11.5 (string-db.org) to create networks using the STRING active interaction sources 'experiments', 'database' and 'co-expression' at a confidence threshold of 0.4 (medium). The resulting network was imported to Cytoscape v3.9.1 (cytoscape.org) for visualization.

LC-MS/MS analysis of lipid mediators

Lipid mediators were extracted from cells by using chloroform:methanol mixture (2:1, v/v) under nitrogen atmosphere at all steps. Lipid mediators were analyzed by LC/MS using Thermo Ultimate 3000 HPLC system coupled on-line to a Q-Exactive Hybrid Quadrupole-Orbitrap mass spectrometer (Thermo Fisher) using a C30 reverse phase column (Accucore, 2.1 mm \times 25 cm, 2.6 μ m particle size, Thermo Scientific). The analysis was performed using gradient solvents (A and B) at a flow rate of 100 μ L/min. All solvents were LC-MS-grade. Solvent A: acetonitrile/water (50/50); Solvent B: 2-propanol/acetonitrile/water (85/10/5). Both A and B solvents contained 5 mM ammonium formate and 0.1% formic acid as modifiers. Gradient method was as follows: 0–40 min, 15–50%

B (linear, 5); 40–130 min, 50–100% B (linear, 5); 130–135 min, hold at 100% B; 135–140 min, 15% B (linear, 5); 140–150 min, 15% B for equilibration. The LC system was Thermo Ultimate 3000 complete with a WPS-3000 autosampler, and column temperature was set at 35°C. Spectra were acquired in negative ion mode at a resolution of 140,000 for the full MS scan in a data-dependent mode. Scan range for MS analysis was m/z 150–1800 with a maximum injection time of 128 ms using 1 microscan. An isolation window of 1.0 Da was set for MS2 scans acquired at a resolution of 17,500. Maximum injection time for MS2 scans was 500 ms for low-level analytes and HCD collision energy was set to 24. Capillary spray voltage was set at 4.0 kV, and ion transfer tube temperature was 320°C. The S-lens RF level was set to 70. Data were acquired and analyzed using Xcalibur 4.2 Quan Browser (Thermo Fisher). All lipid mediator standards were purchased from Cayman Chemicals.

Statistical analyses

Results are expressed as mean \pm SEM. Two-group analyses were performed using unpaired Student's *t* test in GraphPad Prism software. All tests were two-tailed, and a *p*-value <0.05 was considered to indicate statistical significance.

Results

Generation and characterization of the mouse model with fluorescently labeled cutaneous SCs

The skin contains myelin-forming and non-myelin forming (Remak) SCs, the latter type representing the majority of the

cutaneous glia.²⁷ Furthermore, nerve or tissue injuries lead to the switch in SC phenotype from myelinating to the immature, non-myelinating, repair phenotype.²⁸ To best capture Cre recombination across these skin SC states,²⁹ we selected its tamoxifen-inducible expression under Plp1 promoter, whose activity was previously demonstrated in the developing and adult myelinating and Remak SCs,^{30,31} as well as in the repair SCs.^{32,33} Thus, Plp1-CreERT/Rosa26Stop-tdTomato (Plp1-Cre/tdTomato) mice were generated, in which a fluorescent protein (tdTomato) is expressed in the SCs after tamoxifen administration (Figure 1A, Supplementary Fig. S1A-E). Cre recombinase activity was confirmed with IF in isolated peripheral neurons (sciatic and spinal nerves) and dorsal root ganglia (DRG), as well as in lungs, spleen, lymph nodes, small intestine, bone marrow, liver and skin (Figure 1B, Supplementary Fig. S2A, B). Flow cytometry was used to confirm and quantify glia-specific tdTomato labeling in the neurons and several organs by co-staining cell suspensions for SC markers p75^{NTR}, GAP43, and S100 β (Figure 1C, Supplementary Fig. S2C). Using fluorescence-activated cell sorting (FACS), we isolated the population of the cutaneous p75^{NTR}+ tdTomato+ glial cells and confirmed that they expressed SC-associated genes (Figure 2A-C).

RNA-seq analyses of peritumoral vs control cutaneous SCs

Using FACS, we isolated p75^{NTR}+ tdTomato+ psSCs from the peritumoral skin of B16F10 melanoma-bearing mice (Figure 3A) and compared their expression profiles by RNA-seq to cSCs isolated from anatomically matched skin of tumor-free mice. Differentially expressed genes (DEGs) between the

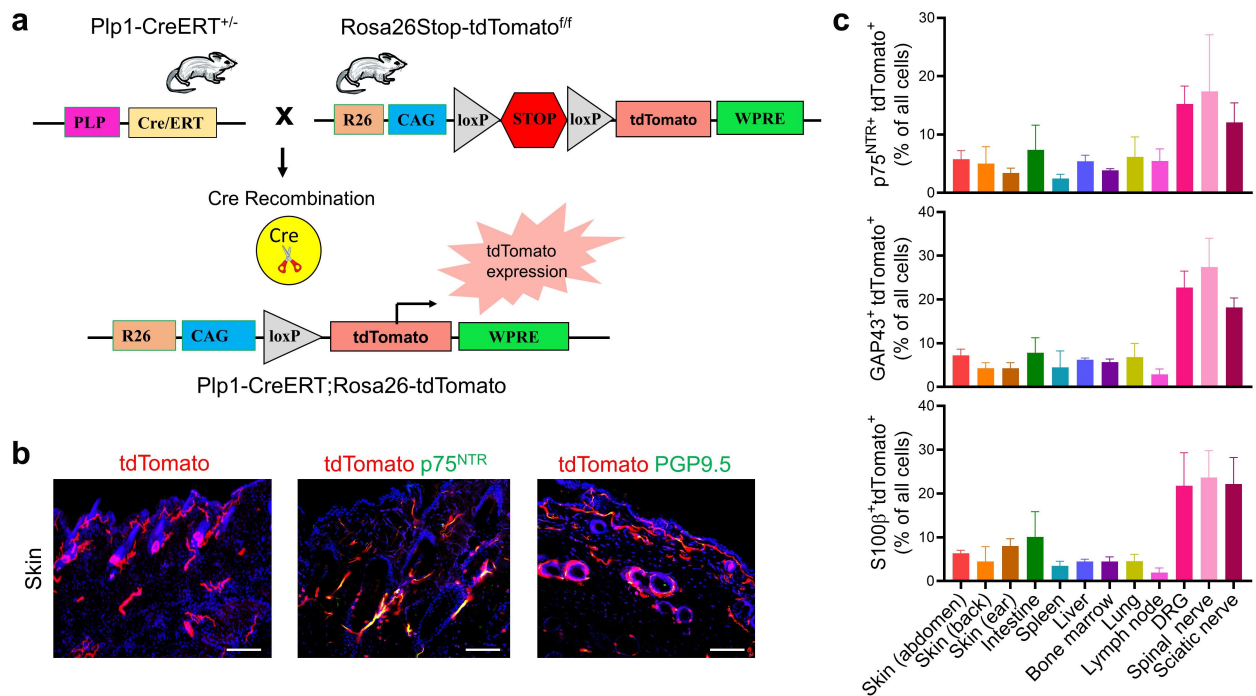


Figure 1. Generation and validation of Plp1-CreERT/Rosa26Stop-tdTomato^{fl/fl} mice. (a) Schematic illustrating the tamoxifen-induced expression of the fluorescent protein (tdTomato) under Plp1 promoter in Plp1-CreERT/Rosa26Stop-tdTomato^{fl/fl} (Plp1/tdTomato) mice. (b) Representative immunofluorescence images of the skin of Plp1/tdTomato mice. Blue: DAPI; Scale bars—100 μ m. (c) Enumeration of p75^{NTR}+ tdTomato+, GAP43+ tdTomato+, and S100 β + tdTomato+ SC populations in different organs of Plp1/tdTomato mice, derived from flow cytometry analyses, and represented as SC percentages of a total number of cells in suspensions. Data are means \pm SEM, *n* = 4 mice.

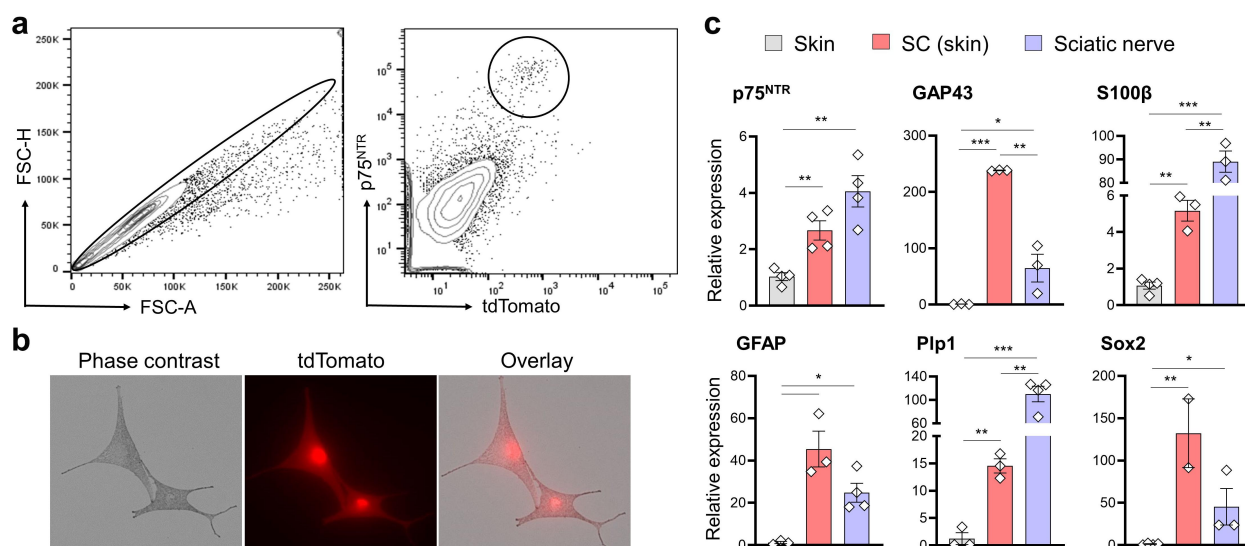


Figure 2. Isolation and characterization of skin SCs from Plp1/tomato mice. (a) Fluorescence activated cell sorting of p75^{NTR}+ tdTomato+ SCs (circle, right panel) from the digested skin of Plp1/tomato mice. (b) Fluorescence microscopy of SCs isolated from the skin of Plp1/tomato mice as shown in a. (c) Relative expression of SC-associated genes measured by RT-qPCR in whole skin (labeled skin), SCs sorted from skin as shown in a (labeled SC skin), and whole sciatic nerves of Plp1/tomato mice. Data are means \pm SEM, two-tailed Student's t test; * $p < 0.05$, ** $p < 0.01$, *** $p < 0.001$.

two groups (Supplementary Table S5) were used in the Ingenuity and Enrichr pathway analyses (Supplementary Tables S6–9). We found that the transcriptional profile of psSCs reflected that of activated (repair-like) glia, compared with cSCs.³⁴ Specifically, we observed enrichment of cell-cycle regulatory pathways, wound healing pathway, signaling by the neurotrophic and other neuron-related factors (NGF, Netrin-1, BDNF, NCAM, Reelin, Semaphorin, Neuregulin, Ephrin receptors), axon guidance pathways, cell migration and extracellular matrix (ECM) reorganization pathways in the psSCs (Figure 3B, Supplementary Fig. S3A). Furthermore, GSEA demonstrated an enrichment of gene sets related to the proliferating embryonic, immature glia (Supplementary Fig. S3B), characteristic of the repair SC cell-cycle entry and dedifferentiation.²⁸ Compared with cSCs, psSCs downregulated genes related to the inflammatory responses, including Th1 activation, interferon signaling, and Toll-like receptor signaling (Figure 3C, Supplementary Fig. S3C), which was also evident in GSEA (Supplementary Fig. S3D). We represented quantitatively the phenotypic reprogramming of psSCs by an integrated transcriptional network, based on RNA-seq derived DEGs (Figure 3D). We verified by IF directly in the skin the upregulation of p75^{NTR} (product of *Ngfr*) by psSCs vs cSCs, an established marker of SC activation in response to nerve injury (Figure 3E, F).³⁵ Our data suggest that SCs of the cutaneous environment adjacent to melanoma tumors transition to an activated, repair-like state, and concomitantly dampen pro-inflammatory responses.

Functional analyses of the immunosuppressive properties of the peritumoral SCs

We next tested the impact of psSCs on anti-melanoma immunity. Splenocytes were isolated from B16F10 melanoma-bearing C57Bl/6 mice and primed *in vitro* with irradiated (IR) B16F10 melanoma cells and interleukin-15 for 7 days (Figure 4A). SCs from the skin adjacent to melanoma

tumors and from the anatomically matched skin of tumor-free mice were isolated by FACS and co-incubated with primed splenocytes and B16F10 cells for 24 hours, followed by interferon (IFN)- γ measurements (Figure 4A). Relative to the splenic immune cells, skin SCs secreted significantly less IFN- γ , and we observed no difference in the production of IFN- γ between psSCs and cSCs (Figure 4B). In the presence of cSCs, splenocytes re-challenged with melanoma cells produced significantly more IFN- γ vs. splenocytes + B16F10 cells (Figure 4B). IFN- γ production by the splenocytes was significantly diminished in the presence of psSCs vs cSCs (Figure 4B). SCs isolated from sciatic nerves of tumor-free and tumor-bearing mice did not enforce the production of IFN- γ by the melanoma-primed splenic immune cells, suggesting that a relatively pro-inflammatory homeostatic state of skin SCs vs. sciatic nerve SCs is reprogrammed locally in the psSCs by the presence of an adjacent tumor but not distally in the SCs of the sciatic nerve.

To delineate the mechanism underlying immunosuppressive functions of melanoma-associated SCs, we examined the top DEGs in the RNA-seq data (Supplementary Table S5). We noticed a strong upregulation of *Alox15* (encoding 12/15-LOX)³⁶ by psSCs vs cSCs (FC = 15.78, $p = 3.1 \times 10^{-9}$). 12/15-LOX enzymes (homologs of leukocyte type 12S-LOX in mice and reticulocyte type 15S-LOX in humans)³⁶ utilize PUFA substrates (primarily the arachidonic acid, AA, in animals) to generate a series of pro- and anti-inflammatory eicosanoids.³⁷ We used LC-MS to perform lipidomic analysis of select eicosanoid lipid mediators produced by SCs which were cultured in melanoma-conditioned medium vs control medium. We found that generation of several pro-inflammatory lipid species, including leukotriene B4 and heptoxilin A3, decreased in melanoma-activated SCs vs. cSCs (Figure 4C). In contrast, anti-inflammatory lipid mediators prostaglandin E2 (PGE2) and lipoxin A4 (LXA4) were produced at significantly higher levels by SCs cultured with melanoma-conditioned medium vs cSCs (Figure 4D). RT-qPCR revealed that both *Alox15* and

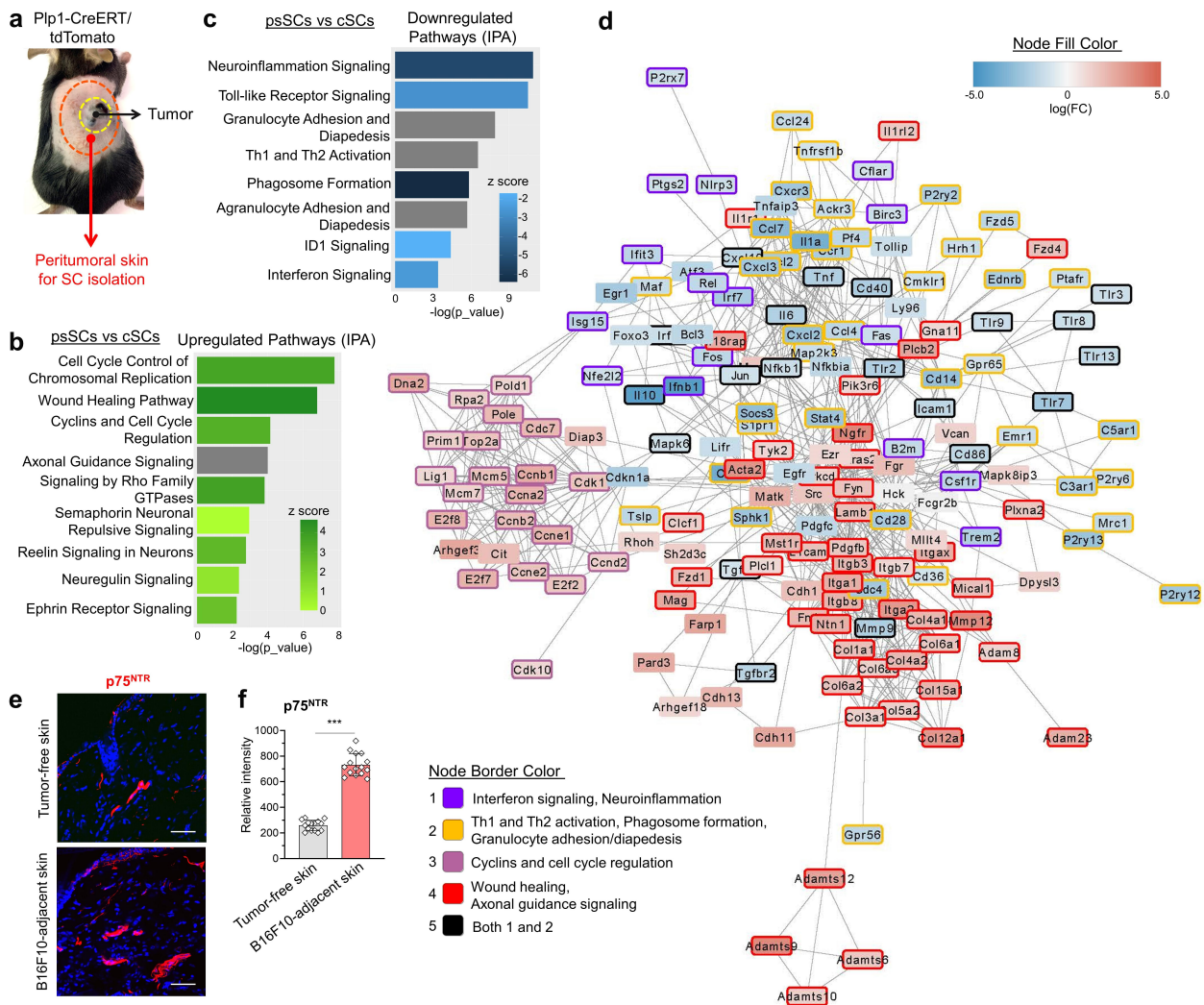


Figure 3. Transcriptional analyses of the peritumoral skin SCs. (a) Schematic of psSC isolation from B16F10-bearing Plp1/tdTomato mice. Ingenuity pathway analyses (DEGs psSCs vs. cSCs), with select top upregulated (b) and downregulated (c) pathways in the psSCs are shown. For each pathway z-score and $-\log_{10}(p\text{-value})$ are indicated unless the z-score could not be determined (gray bars). (d) Network diagram demonstrating the transcriptional reprogramming of the psSC vs. cSCs. Node fill color represents log(fold_change) of gene expression. Node border color represents genes within indicated pathways; $n = 3$ mice/group. (e) IF of p75^{NTR} SCs in the skin of tumor-free C57Bl/6 mice and in the skin adjacent to B16F10 tumors. Blue: DAPI, Scale bars—50 μm . (f) Enumeration of relative fluorescence intensity of p75^{NTR} in tumor-free vs. B16F10-adjacent skin of C57Bl/6 mice, represented as mean intensity over 0.1 mm² visual field; $n = 3$ mice/group $\times 5$ images/mouse. Data are means \pm SEM, two-tailed Student's t test; *** $p < 0.001$.

PTGS2 (encodes COX2) were upregulated in FACS-purified psSCs vs. cSCs as well as in SCs treated with melanoma-conditioned medium vs. cSCs, consistent with our recently published study (Figure 4E, F).²⁶

The biological synthesis of lipoxins involves 12/15-LOX. Lipoxins, similarly to PGE₂, have been shown to limit inflammatory responses via several mechanisms, including by directly reducing Th1 and Th17 effector functions of the T cells.^{37,38} Using ELISA, we confirmed an increase in lipoxin B4 production by SCs cultured in melanoma-conditioned medium, which was abrogated by 12/15-LOX inhibitors (PD146176 and ML351) or by 12/15-LOX deficiency of the SCs (Figure 5A). We next tested the impact of 12/15-LOX inhibition on psSC ability to suppress anti-melanoma effector T-cell activity. Accordingly, the experimental design described in Figure 4A was modified. T-cells were enriched from IL15/B16 (IR)-primed splenocytes (Supplementary Fig. S4) and were used in the final 24 hour co-incubation step with SCs and B16F10 cells. Production of IFN- γ by the melanoma-primed

T cells was significantly reduced in the presence of psSCs vs. cSCs, but not when psSCs were pre-treated with 12/15-LOX inhibitors (Figure 5B). 12/15-LOX and COX2 inhibitors, as well as 12/15-LOX deficiency, also abrogated immunosuppressive activity of the SCs cultured in melanoma-conditioned medium (Figure 5C). A selective antagonist of PGE₂ receptor 4 (EP4), when added to the splenocytes derived from melanoma-bearing mice and co-incubated with B16 cells and SCs, blocked SC-mediated suppression of anti-tumor effector lymphocyte activity (Figure 5D).

We tested by flow cytometry how psSCs co-transplanted with B16F10 cells into the skin of syngeneic immunocompetent mice impact the composition and phenotype of the tumor-infiltrating immune cell population (Figure 6A, Supplementary Fig. S5). Quantities of tumor-infiltrating CD4⁺ and CD8⁺ T cells, as well as T_{reg} and B cells, did not vary between tumors containing psSCs vs cSCs (Supplementary Fig. S6). Among tumor-infiltrating CD4⁺ and CD8⁺ T-cell populations, GzmB⁺ and IFN- γ ⁺ CD4⁺ T-cells and IFN- γ ⁺ CD8⁺ T-cells

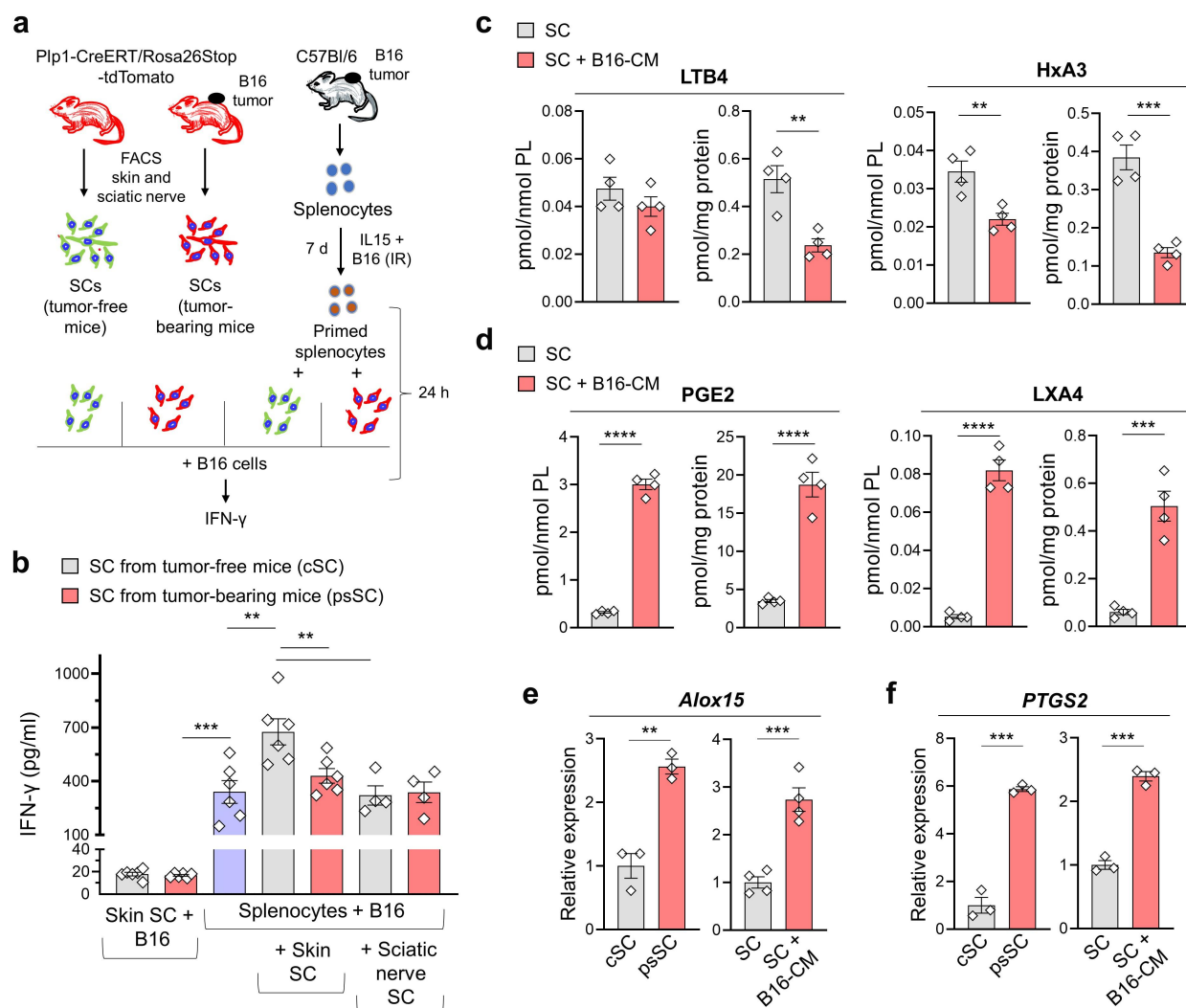


Figure 4. Melanoma-associated SCs upregulate immunosuppressive lipid mediators. (a) Schematic diagram of the experimental design to assay SC impact on the IFN- γ production by the splenocytes primed with B16F10 (labeled B16) melanoma cells. Splenocytes of B16 tumor-bearing C57Bl/6 mice were primed with IL15 + irradiated B16 cells (IR). SCs were purified by FACS from the peritumoral skin (psSC) or the sciatic nerves of B16-bearing or the anatomically matched control skin (cSC) and sciatic nerves of tumor-free Plp1-CreERT/tdTomato mice, and immediately added alone or with primed 10^5 splenocytes to B16 cells. IFN- γ was measured by ELISA after 24 h. (b) IFN- γ production (ELISA) by B16-primed splenocytes \pm SCs + B16 as described in a. (c) Pro- and (d) anti-inflammatory lipid mediators produced by SCs treated with melanoma-conditioned medium (B16-CM) vs. SC + control medium, normalized to total phospholipid (PL) or protein content. Relative expression of *Alox15* (e) and *PTGS2* (f) in the peritumoral skin SCs (psSC) vs. control SCs (cSC), and in SCs incubated in B16F10-conditioned medium (B16-CM) vs. SC + control medium. Data are mean \pm SEM, two-sided Student's t-test; * p < 0.05, ** p < 0.01, *** p < 0.001, **** p < 0.0001.

were present in higher percentages in the tumors containing cSCs vs. those without co-injected SCs (Figure 6B, C). Tumors containing psSCs had significantly fewer GzmB $^+$ and IFN- γ $^+$ cells in both CD4 $^+$ and CD8 $^+$ T cells populations vs. B16F10 + cSCs tumors (Figure 6B, C). Taken together, our results suggest that melanoma-associated repair-like SCs suppress anti-tumor T-cell responses as a result of an altered 12/15-LOX/COX2-dependent lipid oxidation which favors the production of anti-over pro-inflammatory eicosanoids.

Discussion

SCs are now recognized as an important component of the neuronal regulatory network of cancer and anti-tumor immunity; however, analyses of immunomodulatory functions of SCs isolated from tumors and tumor-adjacent tissues are lacking. In the present work, we generated an inducible transgenic model to fluorescently label myelinating, non-

myelinating and repair SCs *in situ*, and developed a FACS-based method to isolate single SCs from the skin and other organs. We show that resident skin SCs adjacent to melanoma tumors undergo phenotypic and functional switching relative to anatomically matched skin SCs of tumor-free mice. These psSCs exhibit features characteristic of repair SCs described in the context of nerve/tissue injury and neuro-regeneration. Our findings are in line with numerous described parallels between tumor stroma and wound healing, and the concept that tumors act as non-healing wounds.^{17,39–41} Specifically, tumor expansion induces tissue injury but arrests the healing process in a state where stromal elements are locked in the execution of wound-resolving programs, which often mechanistically aid cancer progression. There are multiple examples of such functional pro-tumor reprogramming of cancer-associated nonmalignant recruited and tissue-resident cells, including fibroblasts, neutrophils, macrophages, endothelial cells, mesenchymal stromal cells and

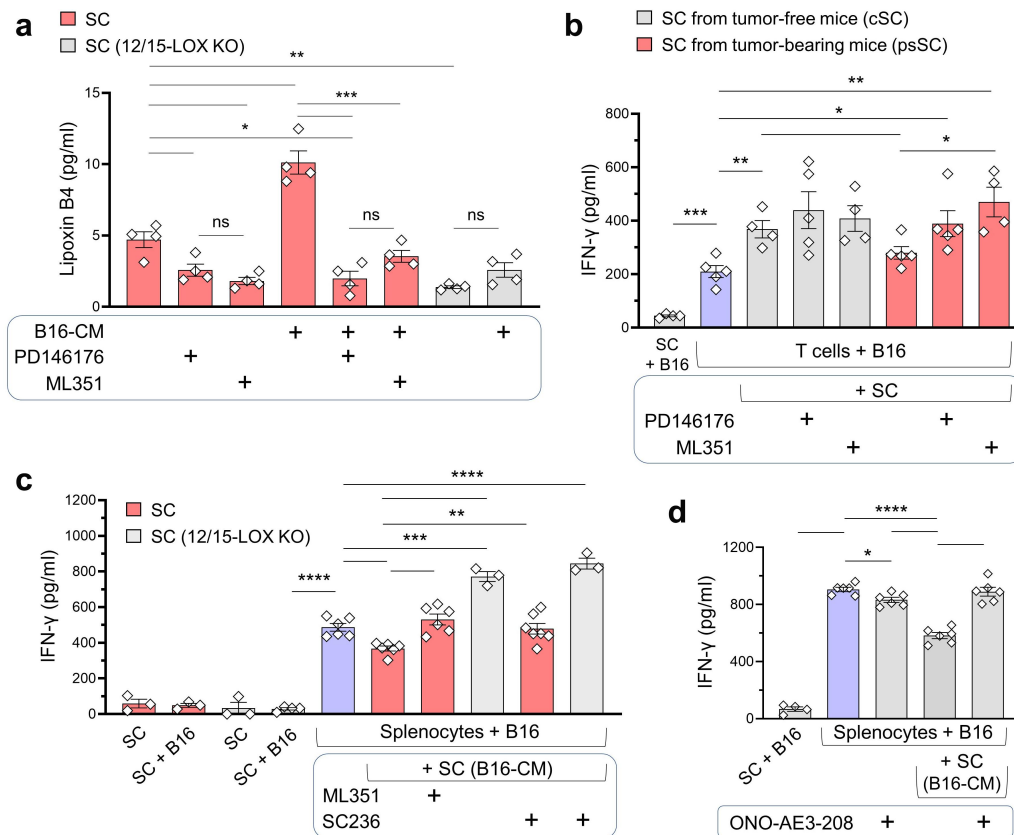


Figure 5. Oxygenated autacoid PUFA metabolites of the peritumoral SCs suppress anti-melanoma T-cell responses. (a) Lipoxin B4 production (ELISA) by SCs isolated from sciatic nerves of C57Bl/6 or 12/15-LOX-deficient mice and incubated in B16-CM or control medium \pm 12/15-LOX inhibitors (PD146176 or ML351). (b) IFN- γ production over 24 h (ELISA) by B16-primed T cells \pm SCs (psSC or cSC). SCs were first incubated with 12/15-LOX inhibitors, washed and added to the T cells. (c) IFN- γ production over 24 h (ELISA) by B16-primed splenocytes \pm SCs from C57Bl/6 or 12/15-LOX-deficient mice. SCs were first incubated in B16-CM \pm 12/15-LOX (ML351) or \pm COX2 (SC236) inhibitors, washed and co-incubation with splenocytes. (d) IFN- γ production over 24 h (ELISA) by B16-primed splenocytes \pm SCs (from B16-CM) \pm EP4 antagonist (ONO-AE3-208). Data are mean \pm SEM, two-sided student's t-test. * p < 0.05, ** p < 0.01, *** p < 0.001, **** p < 0.0001.

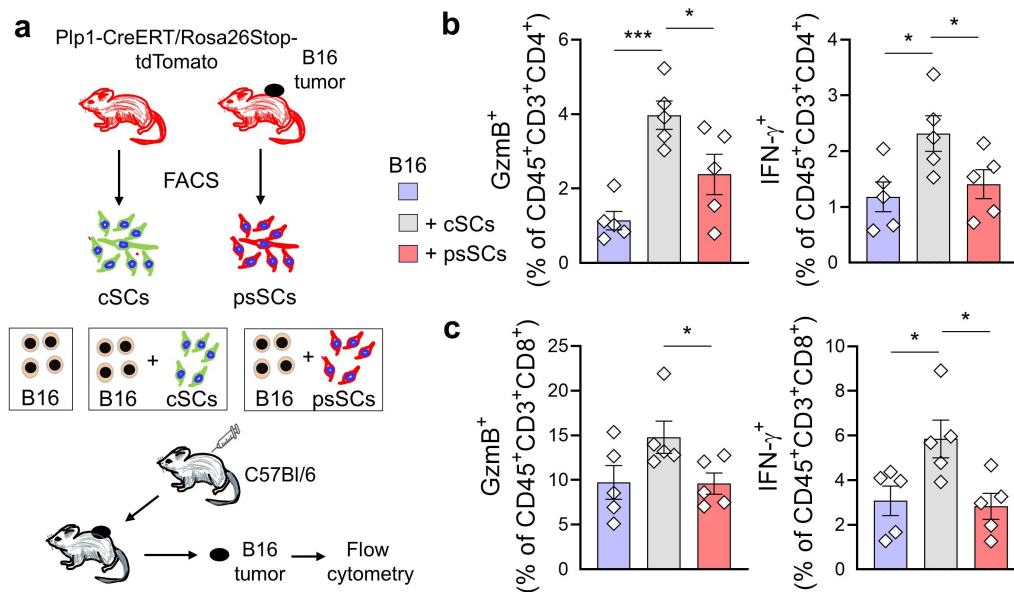


Figure 6. Peritumoral SCs suppress activation of tumor-infiltrating T lymphocytes. (a) Schematic diagram of the experimental design to assay SC impact on the composition and phenotypes of the tumor-infiltrating populations of the immune cells. B16F10 cells (10^5) were injected alone or with freshly isolated psSCs or cSCs (10^4) from Plp1-CreERT/tdTomato mice. Flow cytometry analyses of digested tumors were performed 14 days later. Flow cytometry analyses as described in a, demonstrating that psSCs in tumors decrease intratumoral IFN- γ ⁺, GzmB⁺ CD4⁺ T-cells (b), and CD8⁺ T-cells (c). Data are mean \pm SEM, two-sided student's t-test; * p < 0.05, ** p < 0.01, *** p < 0.001.

others.^{41–44} Here, we show that a similar wound repair-like behavior extends to the SCs of the peritumoral skin.

We previously reported that melanomas may directly activate a nerve-injury response in SCs *in vitro*, and that repair-like SCs support tumor progression.¹⁰ In the current study, we provide evidence that cutaneous SCs at the leading edge of tumor transition to an activated state resembling nerve regeneration. Accompanying such reprogramming is SCs' phenotypic and functional shift which promotes a "cold" tumor microenvironment. While we previously reported that *in vitro* melanoma-activated repair-like SCs chemoattract and polarize myeloid cells to their regulatory/immunosuppressive states,^{11,15,24,25} and promote T-cell exhaustion,²⁶ here we describe immunosuppressive functions of psSCs *in vivo* and *ex vivo*. Mechanistically, we found that tumor-associated SCs significantly upregulate anti-inflammatory (PGE2 and LXA4/B4) and downregulate pro-inflammatory (LTB4 and HXA3) PUFA metabolites and inhibit effector functions of melanoma-primed T-cells in 12/15-LOX and COX-2 dependent manner. Furthermore, we showed that suppression of melanoma-challenged splenic IFN γ -producing immune cells by the SCs occurs via EP4 receptor signaling. These results are consistent with our recent report demonstrating that melanoma-activated SCs upregulate COX2 and increase PGE2 production which polarizes T-cells toward exhaustion phenotype.²⁶ While we show that peritumoral skin SCs suppress anti-melanoma effector T-cell activity, at least in part, with products of enzymatic lipid oxidation, several 12/15-LOX and/or COX2 pathways may result in the production of highly immunosuppressive lipid metabolites. For example, PUFA-phospholipids (–PLs) or lyso-PUFA-PLs may be oxidized by COX2 or 12/15-LOX to PGE2-PLs, which can either act directly on their respective receptors or be hydrolyzed to free PGE2. Future studies will uncover mechanisms regulating these enzymatic lipid oxidation pathways in the tumor-associated SCs.

In this study, we demonstrate direct suppression of melanoma-primed splenocytes and T-lymphocytes by oxygenated lipid metabolites of the peritumoral skin SCs. Tumor-associated SCs likely carry out additional immunomodulatory functions *in vivo* involving innate and adaptive anti-tumor immune responses which impact cancer progression. We and others have previously shown that tumor-associated repair-like SCs are capable, *in vitro*, of stimulating immunosuppressive functions of macrophages, dendritic cells and neutrophils.^{11,15,24,25,45} Future investigations of SC-immune cell interactions *in-vivo* will expand our understanding of locoregional and systemic SC impact on cancer progression. The methodologies we developed and utilized here, including SC purification from multiple organs of the described transgenic mouse model, and the analytical methods of purified SC populations, will facilitate research into immunoregulatory functions of SCs in cancer.

Disclosure statement

No potential conflict of interest was reported by the authors.

Funding

This project was supported by the Research Scholar Grant, RSG-19-088-01-CSM, from the American Cancer Society (YLB), by awards

R01CA266529 (YLB) and R01CA165065 (VEK), and by the Hillman Fellows for Innovative Cancer Research Program funded by the Henry L. Hillman Foundation (YLB). This project utilized the University of Pittsburgh Imaging Core that is supported in part by award P01HL114453, and the Hillman Cancer Genomics Facility and Bioinformatics Services, supported in part by award P30CA047904.

Data availability statement

The RNA sequencing data discussed in this publication have been deposited in NCBI's Gene Expression Omnibus and are accessible through GEO Series accession number GSE208150 (<https://www.ncbi.nlm.nih.gov/geo/query/acc.cgi?acc=GSE208150>).

Significance

Schwann cells have been implicated in cancer progression, but their functions in the tumor microenvironment are unclear. We demonstrate that Schwann cells in the skin adjacent to melanomas are reprogrammed to repair-like Schwann cells which impede anti-tumor T-cell activity by upregulating the production of immunosuppressive eicosanoids.

References

- Zahalka AH, Frenette PS. 2020. Nerves in cancer. *Nat Rev Cancer*. 20(3):143–157. doi:10.1038/s41568-019-0237-2.
- Magnon C, Hall SJ, Lin J, Xue X, Gerber L, Freedland SJ, Frenette PS. 2013. Autonomic nerve development contributes to prostate cancer progression. *Science*. 341(6142):1236361. doi:10.1126/science.1236361.
- Saloman JL, Albers KM, Li D, Hartman DJ, Crawford HC, Muha EA, Rhim AD, Davis BM. 2016. Ablation of sensory neurons in a genetic model of pancreatic ductal adenocarcinoma slows initiation and progression of cancer. *Proc Natl Acad Sci U S A*. 113(11):3078–3083. doi:10.1073/pnas.1512603113.
- Peterson SC, Eberl M, Vagnozzi AN, Belkadi A, Veniaminova N, Verhaegen M, Bichakjian C, Ward N, Dlugosz A, Wong S. 2015. Basal cell carcinoma preferentially arises from stem cells within hair follicle and mechanosensory niches. *Cell Stem Cell*. 16(4):400–412. doi:10.1016/j.stem.2015.02.006.
- Zhao C-M, Hayakawa Y, Kodama Y, Muthupalani S, Westphalen CB, Andersen GT, Flatberg A, Johannessen H, Friedman RA, Renz BW, et al. 2014. Denervation suppresses gastric tumorigenesis. *Sci Transl Med*. 6(250):250ra115. doi:10.1126/scitranslmed.3009569.
- Huang D, Su S, Cui X, Shen X, Zeng Y, Wu W, Chen J, Chen F, He C, Liu J, et al. 2014. Nerve fibers in breast cancer tissues indicate aggressive tumor progression. *Medicine*. 93(27):e172. doi:10.1097/MD.000000000000172.
- Zhou Y, Shurin GV, Zhong H, Bunimovich YL, Han B, Shurin MR. 2018. Schwann cells augment cell spreading and Metastasis of lung cancer. *Cancer Res*. 78(20):5927–5939. doi:10.1158/0008-5472.CAN-18-1702.
- Sroka IC, Chopra H, Das L, Gard JM, Nagle RB, Cress AE. 2016. Schwann cells increase prostate and pancreatic tumor cell invasion using Laminin Binding A6 Integrin. *J Cell Biochem*. 117(2):491–499. doi:10.1002/jcb.25300.
- Silva VM, Gomes JA, Tenorio LPG, de Omena Neta GC, da Costa Paixão K, Duarte AKP, da Silva GCB, Ferreira RJS, Koike BDV, de Sales Marques C, et al. 2019. Schwann cell reprogramming and lung cancer progression: a meta-analysis of transcriptome data. *Oncotarget*. 10(68):7288–7307. doi:10.18632/oncotarget.27204.
- Shurin GV, Kruglov O, Ding F, Lin Y, Hao X, Keskinov AA, You Z, Lokshin AE, LaFramboise WA, Falo LD, et al. 2019. Melanoma-induced reprogramming of Schwann Cell Signaling aids tumor growth. *Cancer Res*. 79(10):2736–2747. doi:10.1158/0008-5472.CAN-18-3872.
- Martyn GV, Shurin GV, Keskinov AA, Bunimovich YL, Shurin MR. 2019. Schwann cells shape the neuro-immune environs

- and control cancer progression. *Cancer Immunol Immunother.* 68 (11):1819–1829. doi:10.1007/s00262-018-02296-3.
12. Demir IE, Kujundzic K, Pfitzinger PL, Saricaoglu OC, Teller S, Kehl T, Reyes CM, Ertl LS, Miao Z, Schall TJ, et al. 2017. Early pancreatic cancer lesions suppress pain through CXCL12-mediated chemoattraction of Schwann cells. *Proc Natl Acad Sci U S A.* 114(1):E85–94. doi:10.1073/pnas.1606909114.
 13. Deborde S, Wong RJ. 2017. How Schwann cells facilitate cancer progression in nerves. *Cell Mol Life Sci.* 74(24):4405–4420. doi:10.1007/s00018-017-2578-x.
 14. Deborde S, Omelchenko T, Lyubchik A, Zhou Y, He S, McNamara WF, Chernichenko N, Lee S-Y, Barajas F, Chen C-H, et al. 2016. Schwann cells induce cancer cell dispersion and invasion. *J Clin Invest.* 126(4):1538–1554. doi:10.1172/JCI82658.
 15. Bunimovich YL, Keskinov AA, Shurin GV, Shurin MR. 2017. Schwann cells: a new player in the tumor microenvironment. *Cancer Immunol Immunother.* 66(8):959–968. doi:10.1007/s00262-016-1929-z.
 16. Roger E, Martel S, Bertrand-Chapel A, Depollier A, Chuvain N, Pommier RM, Yacoub K, Caligaris C, Cardot-Ruffino V, Chauvet V, et al. 2019. Schwann cells support oncogenic potential of pancreatic cancer cells through TGFβ signaling. *Cell Death Dis.* 10(12):886. doi:10.1038/s41419-019-2116-x.
 17. Deborde S, Gusain L, Powers A, Marcadis A, Yu Y, Chen C-H, Frants A, Kao E, Tang LH, Vakiani E, et al. 2022. Reprogrammed Schwann cells organize into dynamic tracks that promote Pancreatic Cancer invasion. *Cancer Discov.* 12(10):2454–2473. doi:10.1158/2159-8290.CD-21-1690.
 18. Stierli S, Imperatore V, Lloyd AC. 2019. Schwann cell plasticity-roles in tissue homeostasis, regeneration, and disease. *Glia.* 67(11):2203–2215. doi:10.1002/glia.23643.
 19. Salvo E, Tu NH, Scheff NN, Dubeykovskaya ZA, Chavan SA, Aouizerat BE, Ye Y. 2021. TNFα promotes oral cancer growth, pain, and Schwann cell activation. *Sci Rep.* 11(1):1840. doi:10.1038/s41598-021-81500-4.
 20. Su D, Guo X, Huang L, Ye H, Li Z, Lin L, Chen R, Zhou Q. 2020. Tumor-neuroglia interaction promotes pancreatic cancer metastasis. *Theranostics.* 10(11):5029–5047. doi:10.7150/thno.42440.
 21. Deborde S, Wong RJ. 2022. The role of Schwann cells in cancer. *Adv Biol.* 6(9):e2200089. doi:10.1002/adbi.202200089.
 22. Fujii-Nishimura Y, Yamazaki K, Masugi Y, Douguchi J, Kurebayashi Y, Kubota N, Ojima H, Kitago M, Shinoda M, Hashiguchi A, et al. 2018. Mesenchymal-epithelial transition of pancreatic cancer cells at perineural invasion sites is induced by Schwann cells. *Pathol Int.* 68(4):214–223. doi:10.1111/pin.12641.
 23. Demir IE, Boldis A, Pfitzinger PL, Teller S, Brunner E, Klose N, Kehl T, Maak M, Lesina M, Laschinger M, et al. 2014. Investigation of Schwann cells at neoplastic cell sites before the onset of cancer invasion. *J Nat Cancer Inst.* 106(8). doi:10.1093/jnci/dju184.
 24. Zhang SH, Shurin GV, Khosravi H, Kazi R, Kruglov O, Shurin MR, Bunimovich YL. 2020. Immunomodulation by Schwann cells in disease. *Cancer Immunol Immunother.* 69(2):245–253. doi:10.1007/s00262-019-02424-7.
 25. Shurin MR, Shurin GV, Zlotnikov SB, Bunimovich YL. 2020. The neuroimmune axis in the tumor microenvironment. *J Immunol.* 204(2):280–285. doi:10.4049/jimmunol.1900828.
 26. Shurin GV, Vats K, Kruglov O, Bunimovich YL, Shurin MR. 2022. Tumor-Induced T cell polarization by Schwann cells. *Cells.* 11(22):3541. doi:10.3390/cells11223541.
 27. Griffin JW, Thompson WJ. 2008. Biology and pathology of nonmyelinating Schwann cells. *Glia.* 56(14):1518–1531. doi:10.1002/glia.20778.
 28. Jessen KR, Mirsky R. 2016. The repair Schwann cell and its function in regenerating nerves. *J Physiol.* 594(13):3521–3531. doi:10.1113/JP270874.
 29. Debbache J, Parfejevs V, Sommer L. 2018. Cre-driver lines used for genetic fate mapping of neural crest cells in the mouse: an overview. *Genesis.* 56(6–7):e23105. doi:10.1002/dvg.23105.
 30. Leone DP, Genoud S, Atanasoski S, Grausenburger R, Berger P, Metzger D, Macklin WB, Chambon P, Suter U. 2003. Tamoxifen-inducible glia-specific Cre mice for somatic mutagenesis in oligodendrocytes and Schwann cells. *Mol Cell Neurosci.* 22(4):430–440. doi:10.1016/S1044-7431(03)00029-0.
 31. Doerflinger NH, Macklin WB, Popko B. 2003. Inducible site-specific recombination in myelinating cells. *Genesis.* 35(1):63–72. doi:10.1002/gene.10154.
 32. Parfejevs V, Debbache J, Shakhova O, Schaefer SM, Glausch M, Wegner M, Suter U, Riekstina U, Werner S, Sommer L. 2018. Injury-activated glial cells promote wound healing of the adult skin in mice. *Nat Commun.* 9(1):236. doi:10.1038/s41467-017-01488-2.
 33. Gomez-Sanchez JA, Pilch KS, van der Lans M, Fazal SV, Benito C, Wagstaff LJ, Mirsky R, Jessen KR. 2017. After nerve injury, lineage tracing shows that myelin and remak Schwann cells Elongate extensively and branch to form repair Schwann cells, which shorten radically on Remyelination. *J Neurosci.* 37(37):9086–9099. doi:10.1523/JNEUROSCI.1453-17.2017.
 34. Weiss T, Taschner-Mandl S, Bileck A, Slany A, Kromp F, Rifatbegovic F, Frech C, Windhager R, Kitzinger H, Tzou C-H, et al. 2016. Proteomics and transcriptomics of peripheral nerve tissue and cells unravel new aspects of the human Schwann cell repair phenotype. *Glia.* 64(12):2133–2153. doi:10.1002/glia.23045.
 35. Meeker RB, Williams KS. 2015. The p75 neurotrophin receptor: at the crossroad of neural repair and death. *Neural regener res.* 10(5):721–725. doi:10.4103/1673-5374.156967.
 36. Singh NK, Rao GN. 2019. Emerging role of 12/15-Lipoxygenase (ALOX15) in human pathologies. *Prog Lipid Res.* 73:28–45. doi:10.1016/j.plipres.2018.11.001.
 37. Tan R, Yan B, Wang C, Zhang L, Mishra SK. 2022. The role of 12/15-Lipoxygenase and its various metabolites generated from multiple polyunsaturated fatty acids as Substrates in Inflammatory Responses. *Biomed Res Int.* 2022:4589191. doi:10.1155/2022/4589191.
 38. Derada Troletti C, Enzmann G, Chiurciu V, Kamermans A, Tietz SM, Norris PC, Jahromi NH, Leuti A, van der Pol SMA, Schouten M, et al. 2021. Pro-resolving lipid mediator lipoxin A4 attenuates neuro-inflammation by modulating T cell responses and modifies the spinal cord lipidome. *Cell Rep.* 35(9):109201. doi:10.1016/j.celrep.2021.109201.
 39. Foster DS, Jones RE, Ransom RC, Longaker MT, Norton JA. 2018. The evolving relationship of wound healing and tumor stroma. *JCI Insight.* 3(18). doi:10.1172/jci.insight.99911.
 40. Hua Y, Bergers G. 2019. Tumors vs. Chronic wounds: an immune cell's perspective. *Front Immunol.* 10:2178. doi:10.3389/fimmu.2019.02178.
 41. Peta KT, Ambele MA, Pepper MS, Zhang X-L. 2021. Similarities between Tumour immune response and chronic wound microenvironment: influence of Mesenchymal Stromal/Stem cells. *J Immunol Res.* 2021:6649314. doi:10.1155/2021/6649314.
 42. Kalluri R. 2016. The biology and function of fibroblasts in cancer. *Nat Rev Cancer.* 16(9):582–598. doi:10.1038/nrc.2016.73.
 43. McFarlane AJ, Fercocq F, Coffelt SB, Carlin LM. 2021. Neutrophil dynamics in the tumor microenvironment. *J Clin Invest.* 131(6). doi:10.1172/JCI143759.
 44. Boutilier AJ, Elsawa SF. 2021. Macrophage polarization states in the tumor microenvironment. *Int J Mol Sci.* 22(13):6995. doi:10.3390/ijms22136995.
 45. Zhou Y, Li J, Han B, Zhong R, Zhong H. 2020. Schwann cells promote lung cancer proliferation by promoting the M2 polarization of macrophages. *Cell Immunol.* 357:104211. doi:10.1016/j.cellimm.2020.104211.